Sensors and Actuators B 191 (2014) 572–578

Contents lists available at ScienceDirect

Sensors and Actuators B: Chemical

journal homepage: www.elsevier.com/locate/snb

Alteration of pore size distribution by sol–gel impregnation for dynamic range and sensitivity adjustment in Kelvin condensation-based humidity sensors

F. Hossein-Babaei [a,*], S. Rahbarpour [b]

[a] Electronic Materials Laboratory, Electrical Engineering Department, K.N. Toosi University of Technology, Tehran, Iran
[b] Electronic Engineering Department, Shahed University, Tehran 159-18155, Iran

ARTICLE INFO

Article history:
Received 21 May 2013
Received in revised form 29 August 2013
Accepted 7 October 2013
Available online xxx

Keywords:
Relative humidity
Humidity sensor
Dynamic range
Pore size distribution
Titanium dioxide
Sol–gel impregnation

ABSTRACT

It has been theoretically established that the dynamic range of sensitivity in porous dielectric ceramic-based resistive or capacitive humidity sensors is mainly determined by the open pore size distribution in their sensing pallets. Here, we directly apply the concept on ceramic resistive humidity sensors and utilize the results for the experimental verification of the theoretical model. The open pore size distribution in a number of identical titanium dioxide pallets, fabricated by the sintering of the slip-cast powder at 1073 K, is modified in two different directions: (a) impregnation with titanium tetraisopropoxide, followed by a heat treatment at 773 K increases the proportion of the finer pores and (b) re-sintering the original pallets at 1223 K closes the finer pores and substantially shifts the distribution towards larger pore dimensions. Sensitivity measurement results are consistent with the theoretically established concept: increasing the population of larger pores heightens the sensitivity to high relative humidity (RH) levels and shifts the dynamic range of the pallets from the original 20–85% to 50–95% RH. On the contrary, increasing the proportion of the finer pores in the microstructure of the ceramic pallet enhances the sensitivity at the lower RH range, shifting the dynamic range of the sensor to the 2–25% RH range.

1. Introduction

The laboratory, industrial, and domestic applications of porous solid-based resistive and capacitive humidity sensors are wide spread. In the most common type of these sensors, the electric conductivity and/or the dielectric constant of a porous ceramic or polymer pallet changes due to the adsorption of the water molecules to its effective surface. These changes are, then, translated to relative humidity fluctuations in the surrounding atmosphere [1]. As a result, the operation mechanism and the quality factors of these devices are strongly dependent on the process of water molecules diffusion into the open pores of the porous pallet and their absorption to the pore walls. The relationship between the pore radius and water adsorption mechanism in a porous solid has been theoretically established more than a century ago by Lord Kelvin:

$$r_k = \frac{2\gamma M}{\rho RT \ln(P_s/P)} \quad (1)$$

wherein, M, ρ and γ are the molecular weight, density and surface tension of water, respectively. P is the partial pressure of water vapor in the surrounding atmosphere and P_s is the saturation pressure of water in the same ambient conditions. Kelvin equation has been verified experimentally by two different optical observation techniques which facilitated direct observation of the surface adsorbed water layers [2,3].

Based on the nature of the porous solid used for pallet fabrication, humidity sensor elements are divided into three main categories of ceramics, polymer and electrolyte [4,5]. Ceramic pallets are of higher physical and chemical stabilities and are advantages from the view point of many quality factors: they are of longer life times [6,7], provide more reproducible RH measurement results [8], can be applied for water content measurements at elevated temperatures [9], and can be recovered after poisoning in a contaminated environment by thermal cleaning [6]. Bulk [10,11] and thin film [12,13] ceramic elements are both utilized for pallet fabrication, but in all configurations the sensing mechanism is based on the measurement of the humidity-sensitive conductivity and/or dielectric constant of the ceramic element.

Humidity sensitive ceramic pallets are mostly made of oxide-based ceramic dielectrics and wide band gap semiconductors such as TiO_2 [14–16], SnO_2 [17,18], $ZnCr_2O_4$ [19,20], Al_2O_3 [21,22] and $MgCr_2O_4$ [23,24]. The physical property monitored in the majority

* Corresponding author. Tel.: +98 21 8873 4172; fax: +98 21 8876 8289.
E-mail addresses: fhbabaei@kntu.ac.ir, fhbabaei@yahoo.com (F. Hossein-Babaei), s.rahbarpour@shahed.ac.ir (S. Rahbarpour).

0925-4005/$ – see front matter © 2013 Elsevier B.V. All rights reserved.
http://dx.doi.org/10.1016/j.snb.2013.10.032

of these pallets is the electrical conductivity (σ) of the pallet, which increases with the RH level in the surrounding atmosphere. In selecting the pallet material, emphasis is on having an efficient physical interaction with the water vapor in the atmosphere and a low, but easily measurable, pallet conductance at zero RH. The former criterion is mainly linked to the mechanism of water layer formation on the effective surface of the solid. The efficacy of this mechanism is quantitatively stated by the contact angle between the solid (metal oxide) and the liquid (water) phases. A close-to-zero contact angle makes the material suitable for pallet fabrication [25]. The latter criterion, however, places a limit on the dry conductivity of the material, as a high room temperature dry electrical conductivity can cover the conductivity increase due to the water vapor adsorption, particularly at low RH levels. The lower conductivity limit is usually dodged by appropriate electrodes shape and size [26] designed to bring the device conductance into the easy-to-measure range.

Despite their many advantages quality factors, the dynamic range of no ceramic pallet affords full RH measurement range. A single pallet is of acceptable sensitivity only within a portion of the 0–100% RH range; above this dynamic range the sensor is saturated and below this range the sensitivity decays to unacceptably low values. In these sensors, according to Kelvin equation, a wider dynamic range is associated with a broader pore size distribution pallet [1,27,28]. Such a pallet should hold an optimum blend of pores ranging from a few nanometers to several microns in diameter. Indeed, porosity, pore size distribution and pore morphology of the ceramic pallet affect many other quality factors, such as response and recovery times, in gas and humidity sensors as they control the process of molecular diffusion of the analyte into the pallet structure, as well [29,30]. Research on design and fabrication of solids with specified pore size distribution for sensing at predetermined RH ranges or broadening of the dynamic range of a particular class of RH sensors is still going on [31]. At the present state of the art, covering the full RH range with a single pallet is impractical [32].

The RH dependence of conductivity in porous solids has been the subject of numerous investigations [33,34], and quantitative relationships between the pore size and the capillary condensation of the water molecules has been theoretically developed since as early as year 1958 [27]. The model suggests that as the RH in the surrounding atmosphere goes down, the condensation of water molecules on the solid surface requires finer pores. Yamazoe et al. have analytically presented a general model for this relationship, which predicts a clear relationship between the pore size distribution in the pallet structure and the dynamic range of its RH sensitivity [4]. The predictions of this model have been verified by the fabrication and characterization of different pallets of different porosity levels and pore size distributions [28]. Here, for the first time, we are reporting the modification of the pore size distribution of a specific humidity sensor ceramic pallet with different means in different directions and observe the variation of the dynamic range of the sensor. The experimental work is carried out on TiO_2 which is one of the most thoroughly investigated wide band gap oxide semiconductors utilized for humidity sensor pallet fabrication, as well [35]. A comparison of the sensor characteristics before and after pore size modification clarified the changes occurred on the sensor dynamic range. We show that these variations are consistent with the predictions of the previously presented model [4].

2. Experimental

2.1. Sample preparation

The material used for ceramic pallet fabrication is TiO_2 powder (MERCK 1.00808.1000) used as purchased from the vender. The

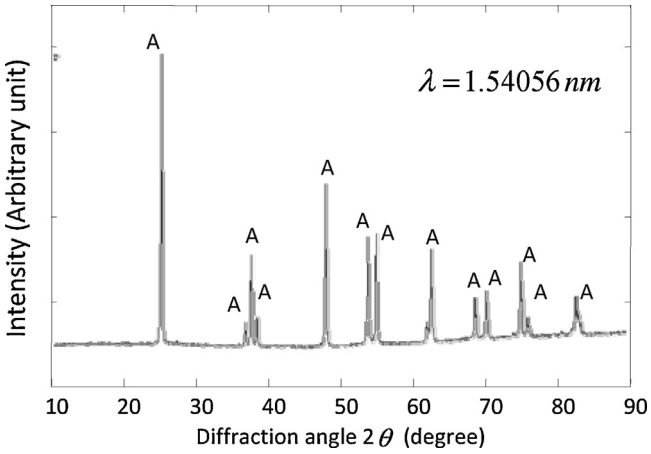

Fig. 1. The XRD pattern obtained from the titanium oxide powder used for pallet fabrication; the pattern contains anatase peaks only.

result of XRD examination, given in Fig. 1, revealed that the material is of anatase phase. No additive, dopant or binder was introduced to the powder during the pallet fabrication process. A viscous slip was prepared by the addition of 40 wt% distilled water to the powder. The slip was dropped as ~12 mg droplets onto the closest point between two unparallel fine, $d = 60\ \mu m$, platinum wires, the ends of which had been spark welded to four refractory metal posts secured in a segment of alumina (Fig. 2(a)). The distance between the two Pt wires is 1 mm as measured at their closest point. The actual inter-electrode distance occurring within the ceramic beads produced, measured after drying and sintering, is ~0.5 mm as observed on the broken beads. The droplet formed a sphere of slip suspending from the Pt wires, which was dried at room temperature and formed an approximately spherical bead (Fig. 2(a)).

The dried TiO_2 ceramic bead along with its all-refractory support structure can entirely be placed in the firing furnace. This method of sample fabrication prevented the loosening and deterioration of the Pt–TiO_2 contacts by unavoidable movements during the forming, drying and sintering processes. Dry beads are sintered at 1073 K for 30 min in a SiC-muffled electric furnace in air and are left in the switched off furnace to cool down overnight. The photograph and a SEM close up of the sample produced are shown in Fig. 2(a) and (b), respectively. The samples prepared according to this process are referred to as N samples.

A second set of the samples, referred to S samples, are prepared by impregnating the N samples with titanium dioxide sol prepared based on titanium alcoxide. The details of the method utilized for the preparation of the alcoxide solution and its conversion to a suspension of TiO_2 nanoparticles is given in Ref. [36]. For impregnation, an N sample is soaked with a sol droplet of a predetermined volume produced at the tip of a liquid sampler. The volume of sol is determined based on the volume of the open pores which are intended to be filled with the sol liquid. The impregnated samples are dried at room temperature and, subsequently, annealed at 773 K in air. The annealing process converts the residues of the dried sol to TiO_2 nanoparticles which precipitate within the open pores of the pallet and modify its pore-size distribution by dividing the large micron-size pores into a number of nanopores. As a result, S samples, compared to N samples, are of lower overall porosity, but their pore size distribution extends deeper into the nanopore region (see below).

A third set of samples, referred to as L samples, is prepared by re-sintering a number of the N samples at 1223 K for another 30 min. Although L samples are of lower total porosity, the grain growth during re-sintering leads to larger grains and, evidently, reduce the population of the smaller open pores. Typical SEM

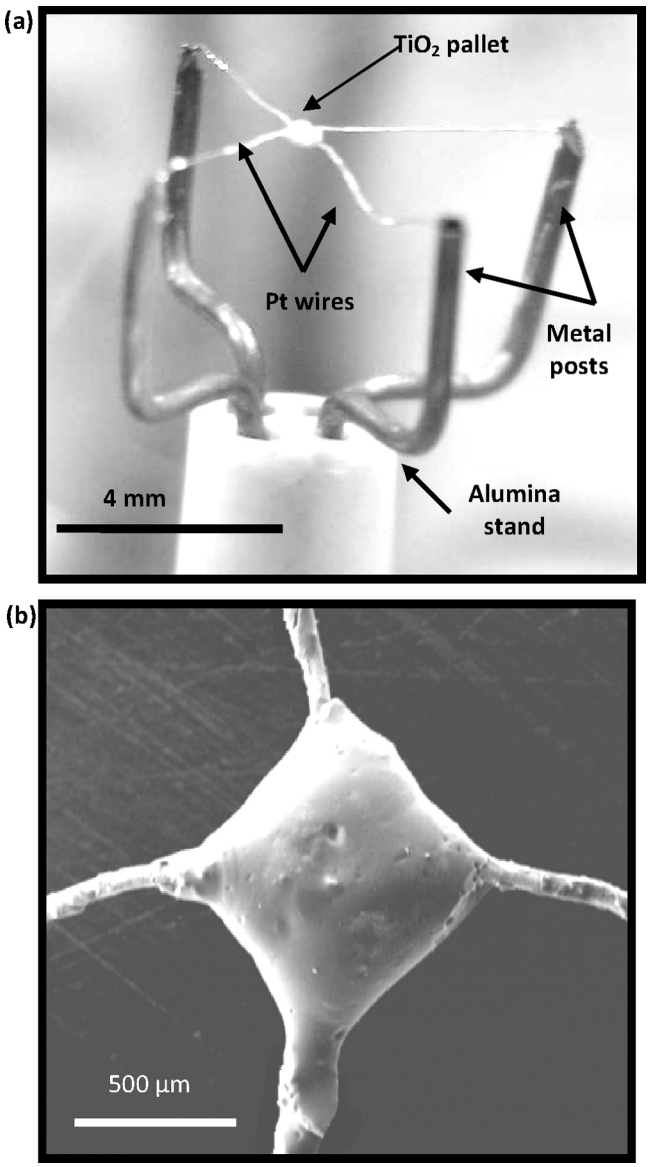

Fig. 2. The photograph of the fabricated ceramic bead humidity sensor (a) and the SEM micrograph of a typical sample fired at 1073 K (b).

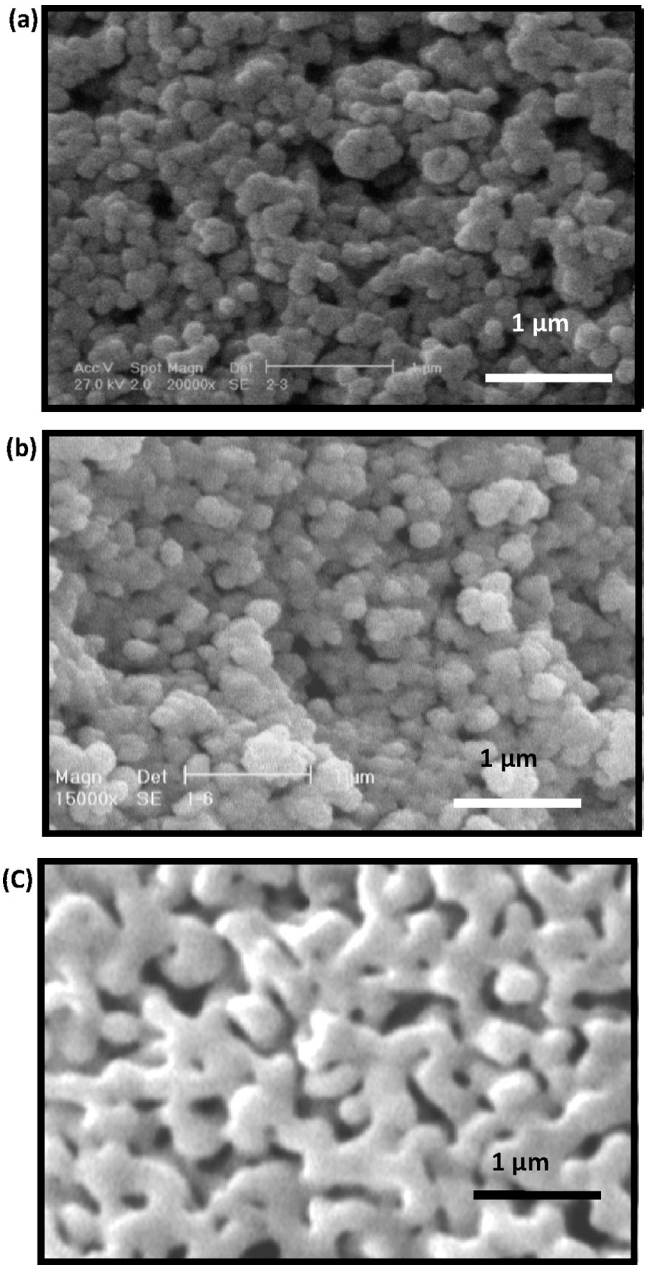

Fig. 3. The SEM micrographs of the fabricated titanium dioxide beads of (a) N (a), S (b), and L (c) types.

micrographs obtained for the TiO_2 beads in N, S, and L samples are given in Fig. 3(a)–(c), respectively, indicating that the porosity and the morphology of the pores have significantly altered by sol–gel impregnation in the S series and over-sintering the L series.

2.2. Characterization

The apparent density of the ceramic pallets is measured by utilizing standard weighing and immersion techniques (ASTM D7263). This parameter is measured on dummy bead samples accompanying N, S and L sample categories prepared and processed via identical fabrication routes. Dummy samples are not connected to wires and these standard tests could be carried out without breaking which can introduce additional errors in the results. The porosity of each sample category was then calculated by comparing its apparent and bulk densities. The effective surfaces of the powdered dummy samples are determined by nitrogen adsorption measurements using Belsorp-mini II system at 77 K. Obtaining reliable pore size-related information from the obtained gas adsorption data is hampered by the type-III nitrogen adsorption isotherm [37] observed for all the sample categories. The results of density, porosity and effective surface measurements are presented in Table 1, indicating higher bulk density and lower total porosity values for the S and L samples compared to those of N samples. The magnitudes of both density and porosity changes in S samples are consistent with the amounts of solid TiO_2 introduced into the bulk by the sol impregnation and subsequent thermal annealing. In case

Table 1
Physical specifications of the three sample categories fabricated. The last two columns are based on the results of nitrogen adsorption measurements at 77 K.

Sample class	Density (g/cm^3)	Porosity (%)	Total area (m^2 g^{-1})	Total pore volume (cm^3 g^{-1})
N	1.4 ± 0.1	70	7.647	0.51
S	1.7 ± 0.1	60	8.086	0.47
L	2.5 ± 0.1	40	2.676	0.30

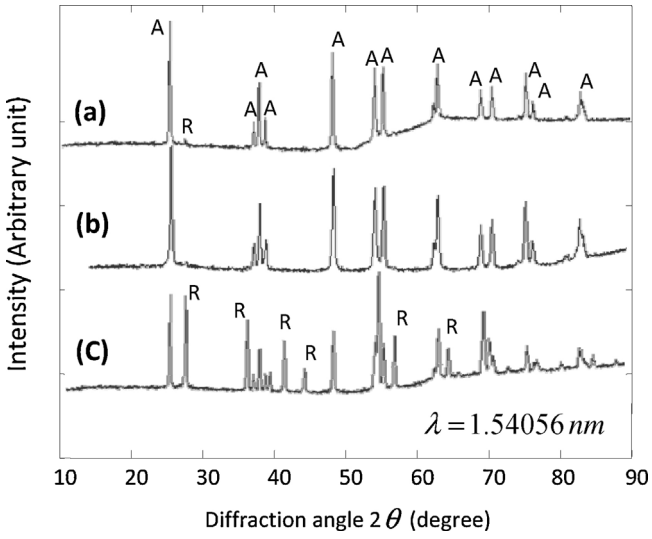

Fig. 4. The XRD patterns obtained for N (a), S (b) and L (c) samples.

of L samples, however, both changes are owing to the extra physical shrinkage and finer pore closure which occur during re-sintering at 1223 K.

The XRD patterns obtained for N, L and S sample categories are given in Fig. 4(a)–(c), respectively. While the starting powder TiO_2 is of anatase phase, all sample categories are anatase-rutile mixtures. The latter phase is the more stable phase of TiO_2 and is produced from anatase at temperatures above 873 K; L samples contain more rutile due to the higher re-sintering temperature utilized. Pore size distributions were estimated based on comparative line averaging among the dummy samples for size and population of the pores on the SEM micrographs obtained from the as broken surfaces of the different dummy samples similar to those shown in Fig. 3(a)–(c). The results are given in Section 3.

The conductance of each sample sensor, measured between two electrode wires, is obtained at different surrounding RH levels at 298 ± 0.2 K. For this measurement, the sample is mounted on a probe which can be inserted into a chamber containing air with a predetermined RH level. The experimental setup is presented in Fig. 5. The temperature at the outer chamber is controlled using

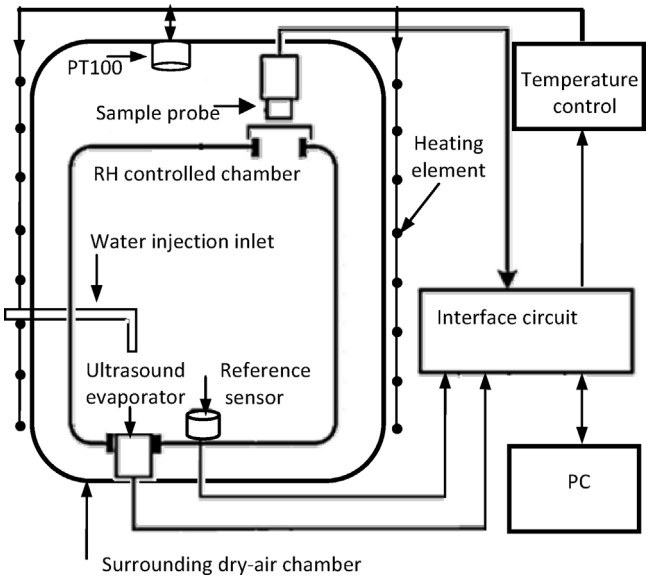

Fig. 5. The schematics of the experimental setup.

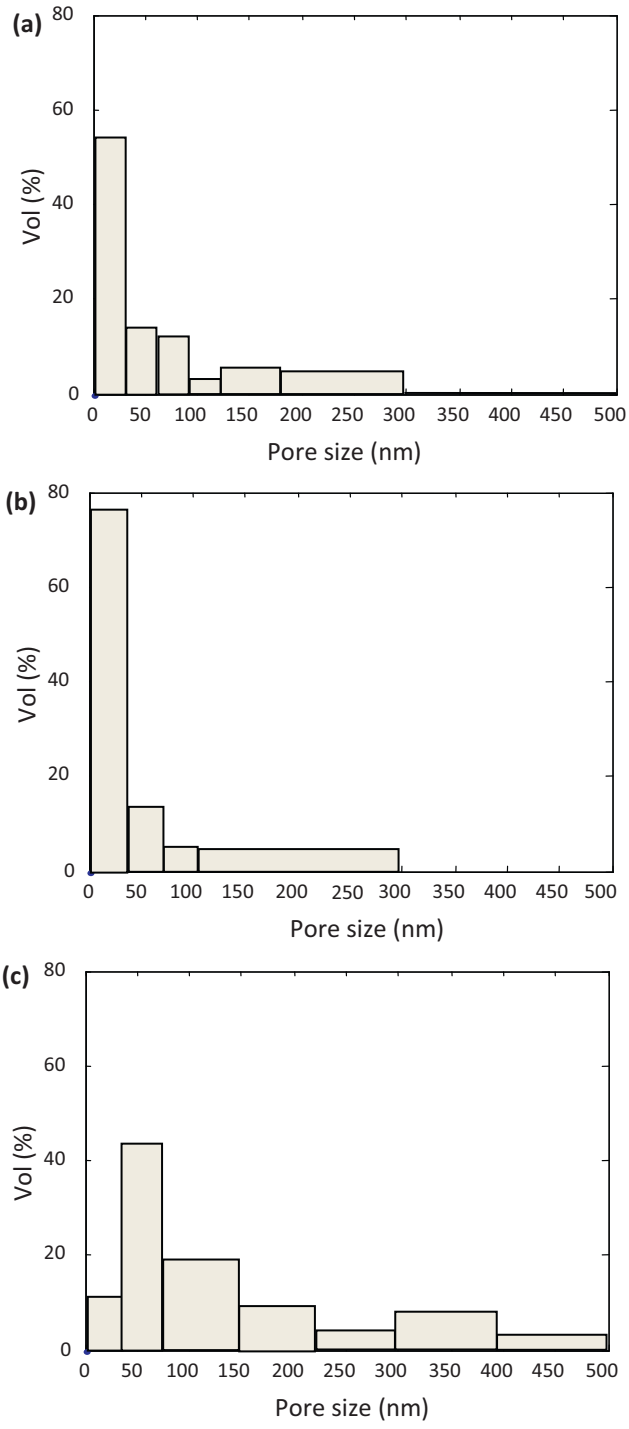

Fig. 6. The estimated pore-size distributions of sample classes (a) N, (b) S, and (c) L.

a system comprising a PT100 temperature sensor, a PID controller connected to a distributed fine wire heating element on the chamber which stabilizes the temperature in the chamber at 298 ± 0.2 K. To minimize the electrode-ceramic connection deterioration due to the electrochemical corrosion, conductance measurements were carried out at 17 Hz. At this frequency, the capacitive admittance of the sample and parasitic capacitors parallel to the sample are insignificant compared to its conductance. Closed chambers of different RH levels, in the range of 2–95%, were obtained by injecting predetermined volumes of distilled water into the dry air (RH = 2%) chamber using a micro-sampler. The injected water was evaporated to obtain the specified humidity level inside the chamber.

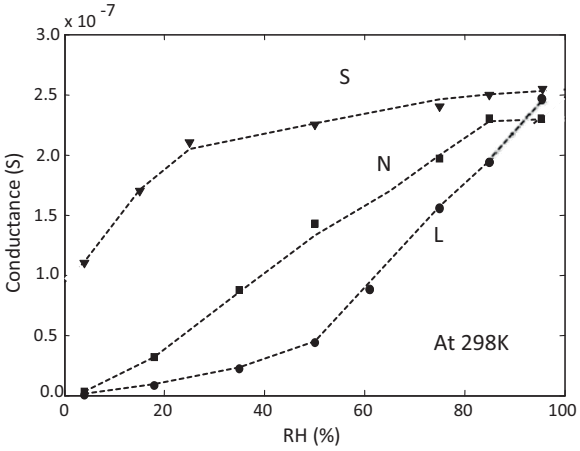

Fig. 7. The electrical conductance of the three sample classes measured in air at different RH levels.

The stable RH levels were monitored by a commercial humidity sensor (HIH 4000) prior to each measurement. The output of reference sensor was calibrated in closed chambers of standard RH levels obtained using different saturated salt solutions [38].

3. Results and discussion

The pore size distributions obtained for samples N, S and L are given in Fig. 6(a)–(c), respectively. The results indicate that compared to N samples, S samples are of higher concentration of the fine open pores while having a lower overall porosity. The latter is owing to the oxide particles grown from the sol material dried and decomposed within the larger pores. The same process increases the population of the fine pores owing to the partial filling of the larger pores and the fact that the solid aggregates produced are composed of nanoparticles and include nanopores. The situation is the other way round in the L samples: many of the fine pores have been eliminated or closed during the excessive growth which occurred in re-sintering leading to a higher density and lower overall porosity compared to N samples. The same process increases the volume percentage of the larger pores of the samples as depicted in Fig. 3(c). Although the population of larger pores increased, the net porosity in L samples is lower than that in the original N-samples due to the overall dimensional shrinkage occurred during re-sintering. These findings are consistent with the experimental data presented in Table 1.

Pallet conductance in air with a specified RH level, G_{RH}, is measured at different RH levels; typical results obtained for the three sample groups are presented in Fig. 7. The conductance of all sample categories measured in vacuum (10^{-5} Torr) is below 10^{-8} S and, hence, the G_{RH} values given in Fig. 7 are almost totally owing to the presence of humid air. Each G_{RH} is recorded after a long stay in the specified atmosphere. According to Fig. 7, $G_{95\%}$ in all samples are almost equal. This is described based on the fact that at close-to-saturation RH levels, almost all the pores are filled with the liquid and the conductance is defined by the geometry of the electrodes. On the contrary, the values obtained for $G_{2\%}$ vary ~100 times among the three sample categories. This stems from the fact that at lower humidity levels, Kelvin condensation occurs in the nanometric pores which are of very different concentrations among different sample categories.

Prior to each transient response measurement, the $G_{2\%}$ of the sample was measured by keeping the sensor for 30 min at RH = 2%; the lowest humidity level utilized. A sudden exposure to a different but constant RH level causes the conductance of the sensor

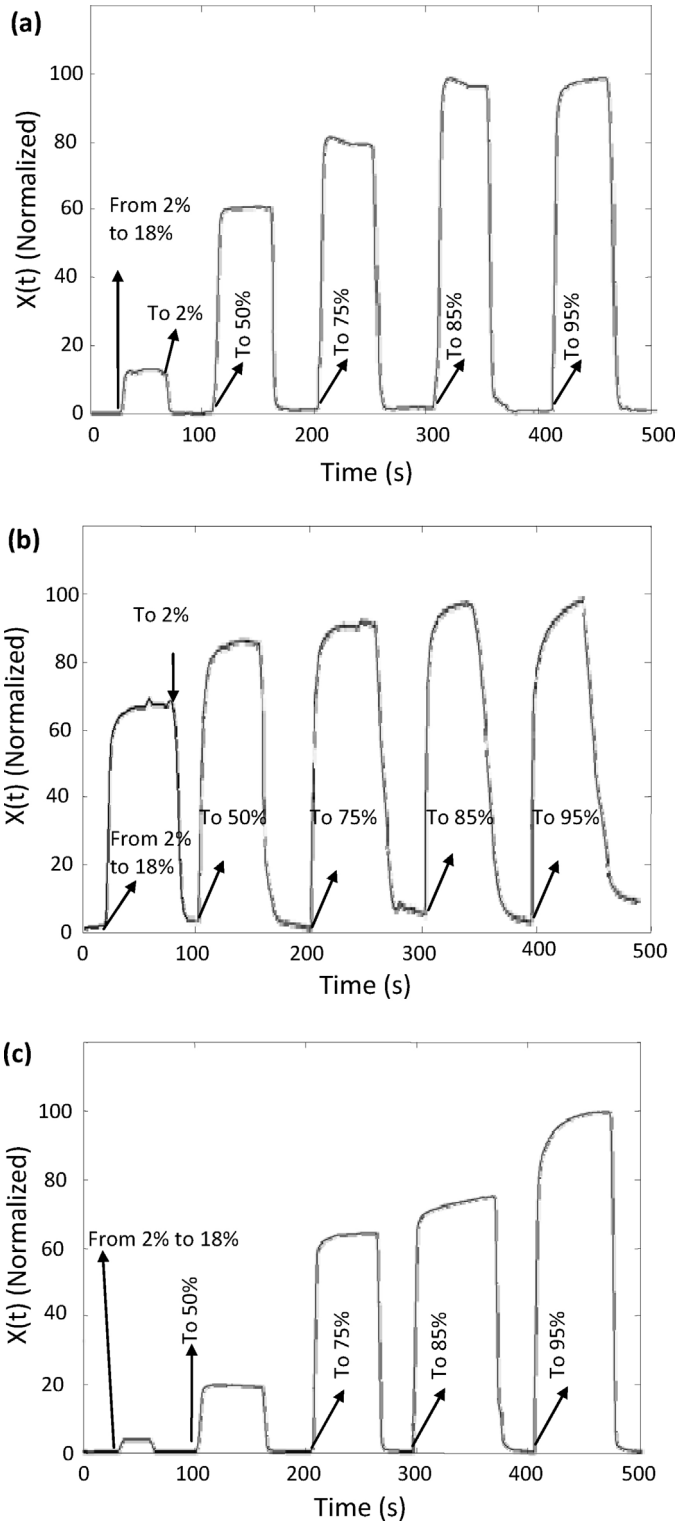

Fig. 8. Normalized transient responses and recoveries recorded for the humidity sensors fabricated based on the pallet classes of (a) N, (b) S, and (c) L depicting the limited, but different, dynamic ranges of the three sample classes.

pallet, $G(t)$, to vary with time. The transient response of the sensor is defined as:

$$X(t) = \frac{G(t)}{G_{2\%}} \quad (2)$$

in which, $G(t)$ is the transient conductance of the sensor. Considering the different, but constant, value of $G_{2\%}$ for each pallet, the $X(t)$

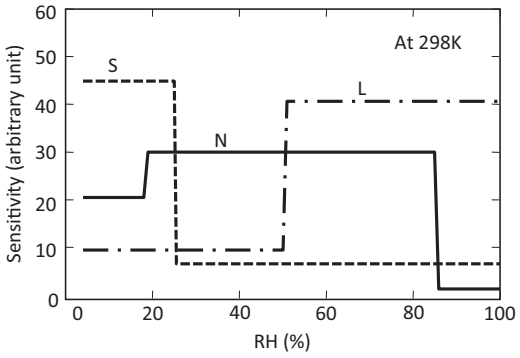

Fig. 9. Comparison of the RH sensitivities estimated based on the experimental data given in Fig. 8 and other similar graphs, for the stated sample classes.

profile related to each sample is, with a change of scale, similar to that of the respective $G(t)$. The normalized transient responses are presented in Fig. 8(a)–(c).

The sensitivity of the sensor around a specified RH, S_{RH} is defined as:

$$S_{RH} = \left.\frac{dG_{RH}}{dRH}\right|_{RH} \quad (3)$$

Due to the nonlinearity of the G_{RH} (RH), as shown in Fig. 7, Eq. (3) results in a humidity level dependent sensitivity, i.e. at around RH_1, the humidity sensitivity of a pallet, S_{RH1}, can be significantly different from that of the same sensor at RH_2. The sensitivities of the different sample pallets are estimated based on the G_{RH} vs. RH diagrams shown in Fig. 7. The results, presented in Fig. 9, depict the dynamic operation ranges of the three different sensor classes, indicating that none of the N, S, and L sample categories can cover the complete humidity range with its dynamic range. The original N samples present a medium RH dynamic range covering from 20% to 80%. In L samples, the dynamic range shifts towards higher RH range of 60–95%, while the S-type pallets demonstrate a shift of dynamic range to lower 2–25% RH range.

For each sample, the response time, the time required for $G(t)$ to ascend from 5% to 95% of its steady-state response level, after a sudden exposure to a higher RH surrounding, and the recovery time, measured in a reverse fashion at sudden RH falls, were measured on the recorded transient responses. Typical normalized response and recovery diagrams related to the three different sample categories are given in Fig. 10. The longer response and recovery times observed in the S-samples are consistent with the expected longer diffuse-in and diffuse-out times of the target molecules [30] into these samples of more intricate pore topography.

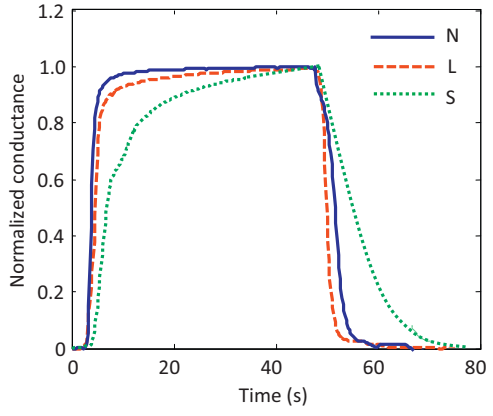

Fig. 10. Normalized response and recovery profiles of the stated pallet classes obtained at the midst of their respective high sensitivity ranges.

4. Conclusion

The pore size distribution in a number of TiO_2 humidity sensing pallets was altered in two opposing directions. This resulted in three categories of sample humidity sensors of identical natures but with different pore size distributions. All the samples underwent the assessments of major sensing quality factors in 2–95% humidity range. The measurement results are consistent with the predictions of the models which describe the humidity sensing process by considering the additional electrical conduction introduced by the network of water layers formed by Kelvin condensation on the effective surface of the porous structure of the dielectric pallets. Particularly, the presented results experimentally verified the predicted relationship between the dynamic range of the sensor and the pore size distribution in humidity sensing pallets for the first time.

References

[1] Y. Shimizu, H. Arai, T. Seyama, Theoretical studies on the impedance-humidity characteristics of ceramic humidity sensors, Sens. Actuators B: Chem. 7 (1985) 11–22.
[2] L.R. Fisher, R.A. Gamble, J. Middlehurst, The Kelvin equation and the capillary condensation of water, Nature 290 (1981) 575–576.
[3] L.R. Fisher, J.N. Israelachvili, Direct experimental verification of the Kelvin equation for capillary condensation, Nature 277 (1979) 548–549.
[4] N. Yamazoe, Y. Shimizu, Humidity sensors: principles and applications, Sens. Actuators B: Chem. 10 (1986) 379–398.
[5] B.M. Kulwicky, Humidity sensors, J. Am. Ceram. Soc. 74 (1991) 697–708.
[6] Z.M. Rittersma, Recent achievements in miniaturised humidity sensors—a review of transduction techniques, Sens. Actuators A: Phys. 96 (2002) 196–210.
[7] M. Li, X.L. Chen, D.F. Zhang, W.Y. Wang, W.J. Wang, Humidity sensitive properties of pure and Mg-doped $CaCu_3Ti_4O_{12}$, Sens. Actuators B: Chem. 147 (2010) 447–452.
[8] Z.Y. Wang, L.Y. Shi, F.Q. Wu, S. Yuan, Y. Zhao, M.H. Zhang, The sol–gel template synthesis of porous TiO_2 for a high performance humidity sensor, Nanotechnology 22 (2011) 275502–275510.
[9] M.A. Hassen, A.G. Clarke, M.A. Swetnam, R.V. Kumar, D.J. Fray, High temperature humidity monitoring using doped strontium cerate sensors, Sens. Actuators B: Chem. 69 (2000) 138–143.
[10] E. Traversa, Ceramic sensors for humidity detection: the state-of-the-art and future developments, Sens. Actuators B: Chem. 23 (1995) 135–156.
[11] I.C. Cosentino, E.N.S. Muccillo, R. Muccillo, Development of zirconia–titania porous ceramics for humidity sensors, Sens. Actuators B: Chem. 96 (2003) 677–683.
[12] X. Chen, L. Rieth, M.S. Miller, F. Solzbacher, Comparison of Y-doped $BaZro_3$ thin films for high temperature humidity sensors by RF sputtering and pulsed laser deposition, Sens. Actuators B: Chem. 148 (2010) 173–180.
[13] C.T. Wang, C.L. Wu, C. Chen, Y.H. Huang, Humidity sensors based on silica nanoparticle aerogel thin films, Sens. Actuators B: Chem. 107 (2005) 402–410.
[14] F. Hossein-Babaei, S. Rahbarpour, Porosity modification for the adjustment of the dynamic range of ceramic humidity sensors, in: 3rd International Conference on Sensing Technology, 2008, Tainan, Taiwan, 2008, pp. 648–651.
[15] L.L. Chow, M.M.F. Yuen, P.C.H. Chan, A.T. Cheung, Reactive sputtered TiO_2 thin film humidity sensor with negative substrate bias, Sens. Actuators B: Chem. 76 (2001) 310–315.
[16] G. Gracia-Belmonte, V. Kytin, T. Dittrich, J. Bisquert, Effect of humidity on ac conductivity of nanoporous TiO_2, J. Appl. Phys. 94 (2003) 5261–5463.
[17] S.P. Yawale, S.S. Yawale, G.T. Lamdhadeb, Tin oxide and zinc oxide based doped humidity sensors, Sens. Actuators A: Phys. 135 (2007) 388–393.
[18] G. Korotchenkov, V. Brynzari, S. Dmitriev, Electrical behavior of SnO_2 thin films in humid atmosphere, Sens. Actuators B: Chem. 54 (1999) 197–201.
[19] M. Bayhan, N. Kavasoğlu, A study on the humidity sensing properties of $ZnCr_2O_4$–K_2CrO_4 ionic conductive ceramic sensor, Sens. Actuators B: Chem. 117 (2006) 261–265.
[20] S. Pokhrel, B. Jeyaraj, K.S. Nagaraja, Humidity-sensing properties of $ZnCr_2O_4$–ZnO composites, Mater. Lett. 57 (2003) 3543–3548.
[21] R.K. Nahar, V.K. Khanna, W.S. Khokle, On the origin of the humidity sensitive electrical properties of porous alumina oxide, J. Phys. D: Appl. Phys. 17 (1984) 2087–2095.
[22] K.K. Mistry, D. Saha, K. Sengupta, Sol–gel processed Al_2O_3 thick film template as sensitive capacitive trace moisture sensor, Sens. Actuators B: Chem. 106 (2005) 258–262.
[23] S.S. Pingale, S.F. Patil, M.P. Vinod, G. Pathak, K. Vijayamohanan, Mechanism of humidity sensing of Ti-doped $MgCr_2O_4$ ceramics, Mater. Chem. Phys. 46 (1996) 72–76.
[24] G. Drazic, M. Trontelj, Preparation and properties of ceramic sensor elements based on $MgCr_2O_4$, Sens. Actuators 18 (1989) 407–414.
[25] A.J. Moulson, J.M. Herbert, Electroceramics, second ed., Wiley, 2003, pp. 215.

[26] M. Urbiztondo, I. Pellejero, A. Rodriguez, M.P. Pina, J. Santamaria, Zeolite-coated interdigital capacitors for humidity sensing, Sens. Actuators B: Chem. 157 (2011) 450–459.
[27] J.H.D. Bore, The Shapes of Capillaries and the Structure and Properties of Porous Material, Butterworth, London, 1958, pp. 68–94.
[28] K. Katayama, K. Hasegawa, T. Takahashi, T. Akiba, H. Yanagida, Humidity sensitivity of Nb_2O_5-dopped TiO_2 ceramics, Sens. Actuators A: Phys. 24 (1990) 55–60.
[29] M.H. Seo, M. Yuasa, T. Kida, J.S. Huh, K. Shimanoe, N. Yamazoe, Gas sensing characteristics and porosity control of nanostructured films composed of TiO_2 nanotubes, Sens. Actuators B: Chem. 137 (2009) 513–520.
[30] F. Hossein-babaei, M. Orvatinia, Analysis of thickness dependence of the sensitivity in thin film resistive gas sensors, Sens. Actuators B: Chem. 89 (2003) 256–261.
[31] J. ShahAuthor Vitae, R.K. Kotnala, B. SinghAuthor Vitae, H. Kishan, Microstructure-dependent humidity sensitivity of porous $MgFe_2O_4$–CeO_2 ceramic, Sens. Actuators B: Chem. 128 (2007) 306–311.
[32] T. Islam, L. Kumar, S.A. Khan, A novel sol–gel thin film porous alumina based capacitive sensor for measuring trace moisture in the range of 2.5–25 ppm, Sens. Actuators B: Chem. 173 (2012) 377–384.
[33] D.U. KimAuthor Vitae, M.S. Gong, Thick films of copper-titanate resistive humidity sensor, Sens. Actuators B: Chem. 110 (2005) 321–326.
[34] F. Hossein-Babaei, V. Ghafarinia, Compensation for the drift-like terms caused by environmental fluctuations in the responses of chemoresistive gas sensors, Sens. Actuators B: Chem. 143 (2010) 641–648.
[35] P.M. Faia, C.S. Furtado, A.J. Ferreria, Humidity sensing properties of a thick-film titania prepared by a slow spinning process, Sens. Actuators B: Chem. 101 (2004) 183–190.
[36] F. Hossein-Babaei, M. Keshmiri, M. Kakavand, T. Troczynski, A resistive gas sensor based on undoped p-type anatase, Sens. Actuators B: Chem. 110 (2005) 28–35.
[37] M. Khalfaoui, S. Knani, M.A. Hachicha, A.B. Lamine, New theoretical expressions for the five adsorption type isotherms classified by BET based on statistical physics treatment, J. Colloid Interface Sci. 263 (2003) 350–356.
[38] A. Carotenuto, M. Dell'Isola, An experimental verification of saturated salt solution-based humidity fixed points, Int. J. Thermophys. 17 (1996) 1423–1439.

Biographies

Faramarz Hossein-Babaei received the B.S. degree in electronic engineering from Amir-Kabir Industrial University, Tehran, Iran, in 1971, and the M.S. degree in materials science and the Ph.D. in electrical engineering from the Imperial College, London, UK, in 1975 and 1978, respectively. He has been Professor of Electronic Materials at the Electrical Engineering Department of K. N. Toosi University of Technology, Tehran, Iran, since 1980, and has been Adjunct Professor at the Department of Materials Engineering, University of British Columbia, Vancouver, Canada from 2002 to 2007. He has founded a number of hi-tech spin-off companies mostly active in the field of high temperature electronic materials and technology. His present research interests include electric heating, electrophoretic deposition of electroceramic materials, microfluidics, metal oxide gas sensors and artificial olfaction. Prof. Hossein-Babaei received the Khwarizmi International Award for his outstanding R and D work on high temperature systems in 2006.

Saeideh Rahbarpour received the B.S. degree from Amir Kabir University of Technology (Tehran Polytechnic), Tehran, Iran in 2003, the M.S. degree and Ph.D. from K. N. Toosi University of Technology, Tehran, Iran in 2005 and 2011 respectively, all in electronic engineering. She is currently assistant professor in Shahed University. Her research interests include the physics of oxide semiconductors and the fabrication and assessment of both Schottky type and chemoresistive gas and humidity sensors.